The role of moisture and salt distribution in the weathering of the medieval cave town of Uplistsikhe, Georgia

Oliver Sass[1*] and Stefanie Heil[2]

Abstract

Knowledge of salt and moisture distribution is a key factor for understanding rock decay at cultural heritage sites. The cave town of Uplistsikhe in Georgia, carved from sandstone in late bronze age to medieval times, suffers from progressive scaling and flaking processes. Multi-method investigations of rock moisture and salt distribution were carried out in order to better understand the patterns of decay. Salt distribution was investigated using drill dust samples and paper pulp poultices; moisture was determined by 2D-resistivity and handheld microwave sensors, supplemented by infrared thermography. The combined results from the different methods revealed a complex pattern of salt and moisture distribution. At most sites, K_2SO_4 (arcanite) and its hydrates dominate, sometimes in combination with $CaSO_4$ (gypsum). At one site (Grandhall), halite (NaCl) and niter (KNO_3) prevail. Sulphates are assumed to be a legacy of air pollution; origin of halite and niter remains unsolved but might be due to concrete reinforcements. Two main sources of moisture were evidenced depending on season and spatial situation: (1) Condensation of air humidity at cool cave backwalls in spring (combined with and aided by salt hygroscopicity), evidenced by 2D-resistivity and infrared thermography; (2) seepage along joints particularly at the cave backwalls and roofs, evidenced by handheld microwave sensors. Further investigations should focus on identifying seepage pathways and on clarifying the origin of destructive halite and nitrates.

Keywords Rock-hewn heritage, Rock moisture, Salt distribution, 2D-resistivity, Microwave, IR thermography

Introduction

Moisture and salts cause considerable damage to built and rock-hewn heritage [1]. Rock-cut or cave sites in sandstone worldwide suffer from progressive decay (e.g. [2, 3]). Besides external disturbances such as landslides and seismic activity, the main reasons are fluctuations in temperature and moisture [4] and the destructive effects of salt weathering [5, 6]. Knowledge of salt and moisture distribution is one of the key factors for understanding decay patterns and processes and for designing protective measures. However, detecting and quantifying salt and in particular moisture in stonework is still challenging [1, 7].

In the cave town of Uplistsikhe (Georgia), carved from sandstone in several periods of time from late bronze age to medieval times, widespread scaling and flaking are observed and there are concerns about stability of some of the vaulted ceilings. Different input paths of moisture have to be considered, e.g. condensation of air humidity [8, 9], wind-driven rain or rainwater run-off [10] and capillary rise of ground water [7, 11]. Efflorescent salts may be partly geogenic in origin or be added hydrologically by rising damp [11], meteorologically by salt spray [12] or air pollution [13, 14] and by anthropogenic sources

*Correspondence:
Oliver Sass
oliver.sass@uni-bayreuth.de
[1] Department of Earth Sciences, University of Bayreuth, Universitätsstr. 30, 95447 Bayreuth, Germany
[2] Department of Geography, University of Graz, Heinrichstr. 36, 8020 Graz, Austria

like road salt [15]. Knowledge of input paths, distribution and dynamics are required for monument protection, as wrong treatments (e.g. surface sealing) are known to be potentially ineffective or even harmful (e.g. [16]).

We carried out a multi-method measuring campaign to assess the distribution of rock moisture and salts in selected caves of the Uplistsikhe site as an aid for the implementation of conservation measures. To this end, different types of salt sampling and moisture measurements were carried out in the period between 2018 and 2022, including geoelectrical investigations, handheld microwave sensor measurements, drilling and salt sampling. The work was part of a PhD project without external funding. The aims were:

– To assess spatial distribution and nature of salts at the walls of the caves;
– To assess spatial distribution and origin of wetness;
– To relate weathering damage to salts, temperatures and water, and provide strategies do reduce damage.

The distribution patterns found, as well as the effectiveness of the methods used, are also of interest for similar investigations beyond the local case study.

Study site

The Uplistsikhe cave town and fortress is situated in the Transcaucasian Depression of Georgia, some 10 km east of the town of Gori. The settlement was already a religious and political centre in the Hellenistic period; however, the town was in its heyday in high medieval times (ninth—eleventh centuries) and was abandoned in the thirteenth century [17]. The rock-hewn site covers almost eight hectares on a rocky slope with a vertical cliff overlooking Mrtkvari (Kura) river. Most of the caves are devoid of decoration apart from niches in the back or side walls. Some of the larger structures have coffered tunnel-vaulted ceilings. The cave town was carved out of soft, medium-grained Lower Miocene sandstone series assigned to the Upper Uplistsikhe Subformation [18]. The rock appears homogeneous, but varies in small-scale grain size and colour (from yellowish to medium grey). The matrix is partly calcareous and partly consisting of idiomorphic quartz crystals. According to samples collected and investigated by the authors, open porosity varies between approx. 13–20%.

Climate in Gori is subhumide (mean annual air temperature: 16 °C, annual precipitation 500–550 mm) with warm summers (around 28 °C) and moderately cool winters (around 4 °C) [19]. Rain falls all year with peaks in spring / early summer and a weaker peak in autumn. Snowfall and severe frost are rare.

Widespread weathering features include scaling and flaking of the stone up to mm-thickness both at the interior and exterior of the caves (Fig. 1). At ledges and overhangs outside of the caves, blistering of up to several cm thickness is found (terminology according to [20]). Salt efflorescence is frequent on surfaces that are subject to
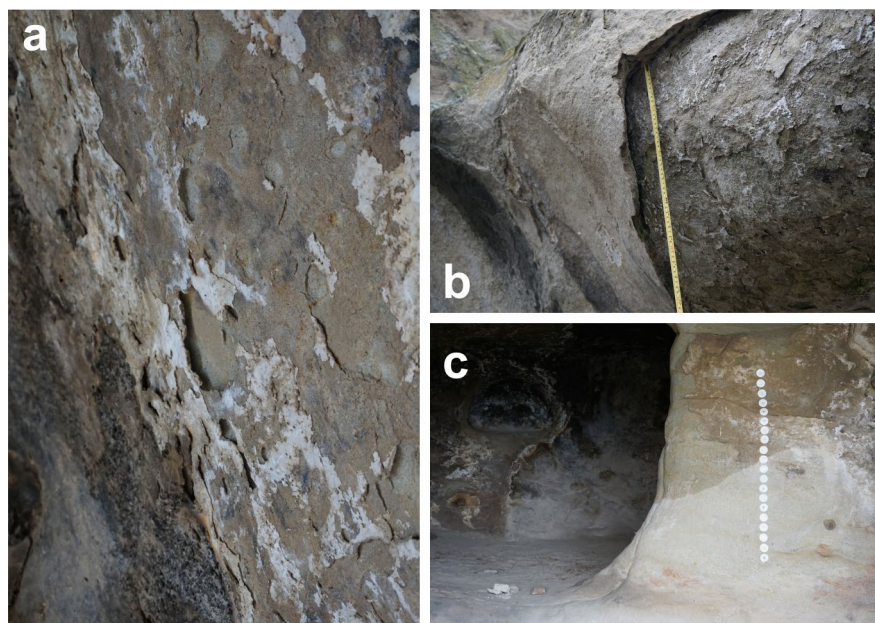

Fig. 1 **a** Widespread flaking in mm-thickness (GH); **b** Blistering up to several cm thickness (between GH and TE); **c** Salt efflorescence (back wall and right side, GH), line of adhesive electrodes of ERT-profile "GH outer recess"

scaling and flaking, and is also found on surfaces from which cm-thick slabs have come off.

We chose four exemplary sites for our investigations: Grand Hall (GH), Longhall (LH), Blackberry Hall (BH) and Teatron (TE) (see Fig. 2). The innermost chamber of GH is carved roughly 5–6 m deep into the rock and measures approx. 4×3×2 m. The rear wall and ceiling show flaking and salt efflorescence; the walls were visibly moist in the first period of field work (March 2018). The first working hypothesis was that the moisture derives from condensation as well as from capillary rise and from not exactly localisable water pathways in the upper part of the rear wall. LH is wider and less deep; the rock appeared to be drier and in the outermost niche (approx. 3 m deep) the rock appeared widely undamaged.

Blistering and salt efflorescence are found mainly at the weather-exposed rock to the side of the cave and above. BH is a wide cave with moderate salt efflorescence in some places and noticeable black crusts at the ceiling of the innermost chamber. These are probably due to open fire by shepards who used some of the caves as a temporal shelter after the abandonment. TE stands out for its vaulted ceilings; salt efflorescence and flaking are present at the back wall and ceiling. In all caves, we named the exact study sites "back wall" if they were in the innermost chamber, "outer recess" further outside in semi-open niches and "outside" if they were at the front of the facades without roof above (see Fig. 3). Circulation and air exchange decrease from the outside and the recesses to the deeper chambers.
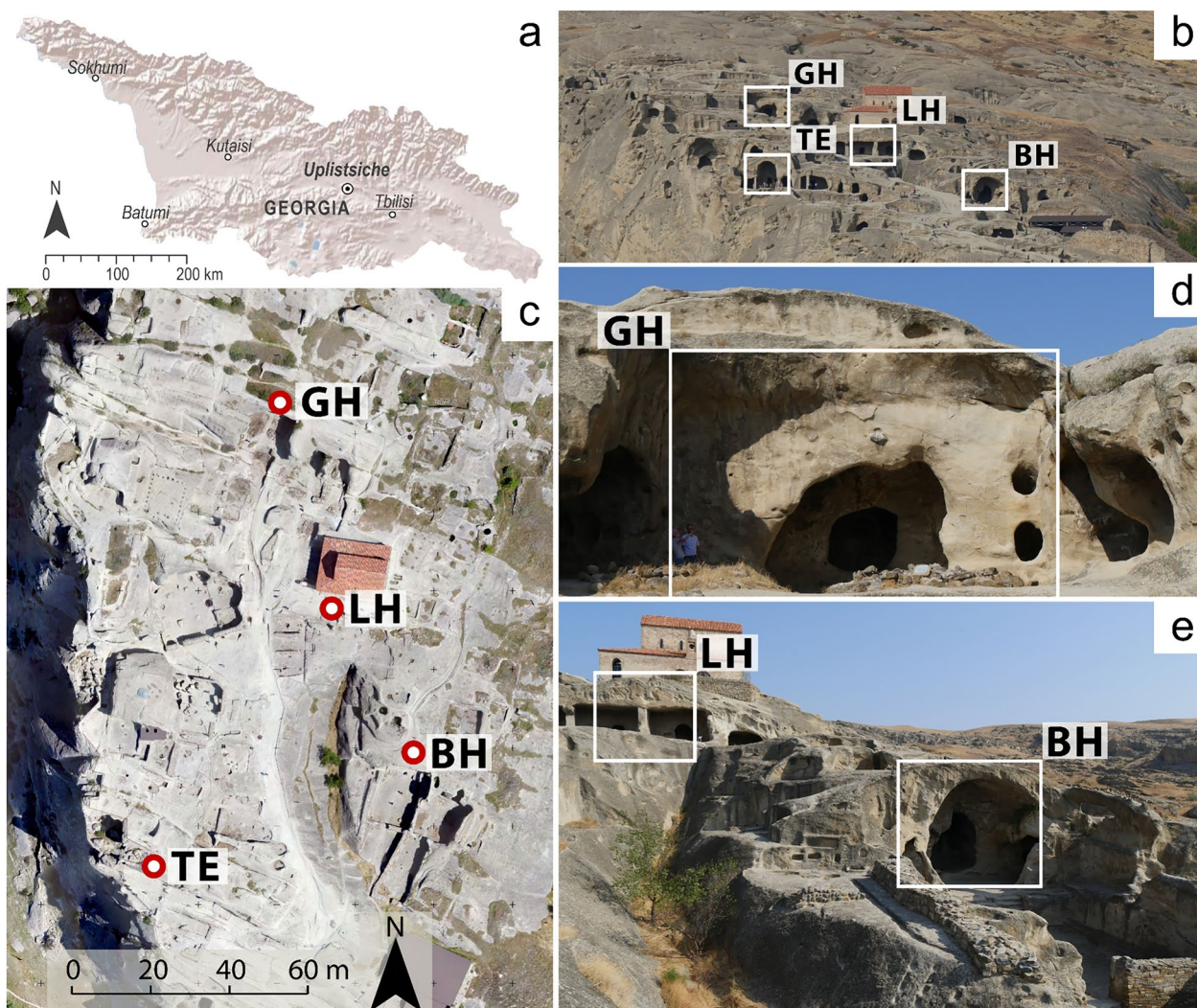

Fig. 2 Uplistsikhe study site. **a** Location within Georgia; **b** Photo from a distance, Grand Hall (GH), Longhall (LH), Blackberry Hall (BH) and Teatron (TE) are marked; **c** Aerial view of the site with investigated caves marked; **d** Grand Hall; **e** Longhall and Blackberry Hall
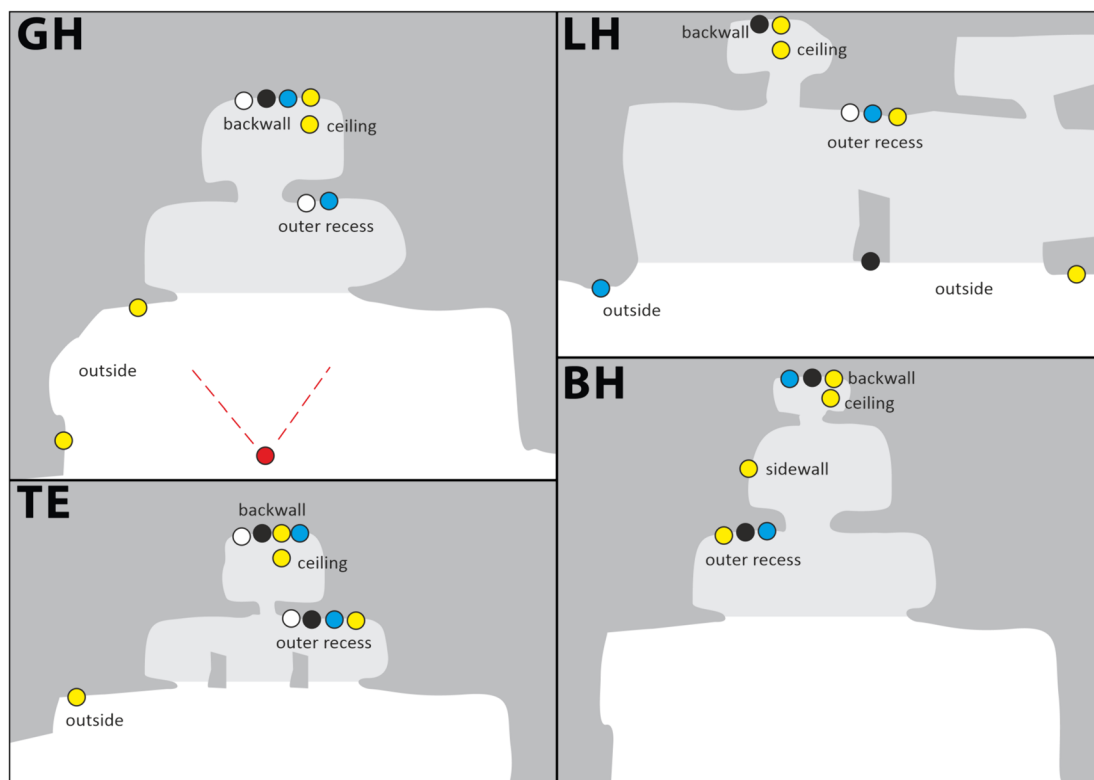
Fig. 3 Ground plan sketch of the four study sites Grand Hall (GH), Longhall (LH), Blackberry Hall (BH) and Teatron (TE). Black: Drill dust sampling; white: paper pulp poultices; blue: 2D-resistivity; yellow: microwave hendheld sensors; red: infrared thermography with approximate field of view. Positions of the points are schematic as at backwalls and outer recesses, measurements were overlapping

Methodology

Field work was carried out in March 2018 and in July 2019, respectively. A third campaign planned for 2020 had to be cancelled due to travel restrictions during the Covid pandemic. Final work could not be done until the autumn of 2022. Before the start and during the investigations, photographs were taken of all investigated sites (GH, LH, BH, TE) and the weathering features were described following the terminology of [20]. Drill dust was collected from boreholes and loose flakes were sampled; both were lab-analysed for salt ions. Additional salt sampling was carried out by means of Paper Pulp Poultices. 2D-resistivity profiles were measured to assess moisture and salt distribution in 2D-sections. Handheld microwave sensors were used to determine spatial distribution of moisture. Additionally, at GH, spatial distribution of temperature (mean and fluctuations) was measured through two Infrared Thermography 24-h monitoring campaigns. Weather was cool and moist with recurrent rainfalls in March 2018, warm and moderately wet with infrequent rainfall in July 2019 and warm and dry in October 2022.

Paper Pulp Poultices (PPP)

PPP are patches of wet cellulose fibres that are placed on the stone as a non-destructive salt sampling method. The poultices allow to extract salts from the near-surface stonework and thus to assess the spatial distribution and type of salts [21, 22]. We used the cellulose fibre material Arbocell BC1000 [23] and formed each poultice from 4 g of cellulose fibres and 20 ml of deionised water (pulp-to-water weight ratio about 1:5).

The PPP were applied at GH backwall and GH outer recess (both: 5×7 points), LH outer recess (5×6 points), TE backwall (6 points along a vertical line) and TE outer recess (7 points along a vertical line); in total 112 patches were applied. The poultices were applied for 120 min to the sampling points. After that, they were removed and allowed to dry completely at ambient temperature and humidity in open plastic bags. Later in the laboratory, the material of each dried poultice was mixed, 2 g were taken and dissolved with 50 ml of deionized water in a magnetic stirrer. The saline solution was filtered and conductivity was measured at 21 °C room temperature [24]. A conductivity sensor (WTW Cond 315i; measurement

accuracy: 0.5% at 0… 35 °C) was used which provides a very good proxy for the total salt content of the sample [22]. As very soluble salts are extracted easier than less soluble ones, certain salts may be underrepresented. However, in the PPP approach we only used total conductivity without differentiating the salt types.

Rock sampling
At a total of seven positions (black dots in Fig. 3), boreholes of 10 mm diameter and 12 cm deep were drilled. At GH backwall there was an upper drillhole (GH-bw-upper) approx. 1.8 m above ground and a lower drillhole (GH-bw-lower) approx. 0.5 m above ground. The drill dust was carefully collected incrementally in intervals of 1.5 and 3 cm (0–1.5 cm, 1.5–3 cm, 3–6 cm, 6–9 cm, 9–12 cm). Additionally, a total of 13 detached surface fragments were sampled across the four sites.

For each sample, 1 g of drill dust (or grinded fragments) was immersed in 50 ml of distilled water by 1 h shaking plus 1 h ultrasonic mixing, and filtered. Six anions (Br^-, Cl^-, NO_3^{2-}, NO_2^{2-}, PO_4^{3-}, SO_4^{2-}) and five cations (Ca^{2+}, K^+, Mg^{2+}, Na^+, NH_4^+) were analysed by ion chromatography (IC) with the IC system Dionex ICS 5000 in the Oxford Resilient Buildings and Landscapes Lab. Of these ions, only Cl^-, NO_3^{2-}, SO_4^{2-}, Ca^{2+}, K^+ and Na^+ were considered further as the concentration of the others was 1–2 magnitudes lower.

Results were analysed using the open RUNSALT software [25, 26] which assesses probable salt types that crystallize from complex salt brines as well as their respective deliquescence points based on thermodynamic models. RUNSALT also calculates the volume of the crystallized salts at each environmental condition (temperature and RH). The charge imbalance of the ion analysis was corrected by a proportional autobalancing method. This charge imbalance may derive from analytical error or the absence of particular ions in the chemical analysis [27]. Volume increase values were converted to the entire sample by multiplying with the percentage of the respective salts in the sample, to assess how significant the crystallization process is in terms of rock decay. We are aware of limitations and pitfalls with RUNSALT such as incorrect charge autobalancing and inconsistencies related to single salts [27].

2D-resistivity profiling (ERT)
2D-resistivity is a geophysical technique for determining the distribution of electrical conductivity in the subsurface. Constant current is fed in via two current electrodes and the resulting potential is taken through two voltage electrodes. By combining different electrode positions and spacings along a line of electrodes, a 2D image of the subsurface can be calculated [28]. As conductivity in porous rock depends on amount and salinity of pore water [29], conductivity distribution is a proxy for dampness of the stone; in very highly conductive zones the presence of soluble salts can be supposed. We used a GeoTom device (Geolog2000, Augsburg/Germany) equipped with individually manufactured shielded cables with crocodile clips for up to 50 electrodes. Self-adhesive medical (ECG) electrodes were used to establish electrical contact to the walls without damaging the historical rock surfaces [1, 30]. The round stickers of the electrodes have a diameter of 4 cm with a 0.8 cm spot of conductive silicone gel in the middle. When contact problems occurred at single electrodes, a few drops of water were carefully dribbled behind the sticker, which was usually enough to reduce contact resistivity without distorting the results.

Electrode spacing depended on height and topography of the walls. We chose 6 cm spacing and 35 electrodes in most cases, always arranged in a vertical line, resulting in a total profile length of 2.04 m. We used the Wenner configuration which provides a good signal–noise ratio and is favourable for detecting surface-parallel structures [31, 32]. Penetration depth in this setting is roughly 1/6 of the profile length, i.e. approx. 35 cm. On strongly relieved or curved walls, the topography was recorded by manually measuring the distances to a straight wooden batten and included in the inversion routine. For data inversion we used the Res2DInv software [33]. Our settings include a robust inversion routine and resolution enhancement by quadrupling the number of calculation nodes. The results were then exported to spreadsheets and analysed further (e.g. deriving averages at certain depth levels). Spatial patterns and resistivity changes were visualized in isoline plots using Surfer® software.

We measured eight vertical ERT profiles in March 2018 and repeated the measurements in July 2019. Two profiles were measured at each of the four investigated caves, one in the innermost cave (not possible at LH), and one outside or in the outer recess. Due to the dry rock and according contact problems, one profile in 2018 and four in 2019 had to be discarded (Table 1). RMS errors of the accepted profiles ranged from 1.2 to 9.9%. Calibration from conductivity to rock water content (RWC) was determined in lab measurements (see section below).

Handheld microwave sensors (MW)
Microwave measurements of moisture are based on the principle that the complex dielectric constant (ε) of water is much higher than that of dry materials (e.g. [34]). In the frequency range of 1–10 GHz it is assumed that the influence of pore water salinity can be neglected [35] which is a great advantage compared to all sensor types working with electrical conductance. Handheld sensors

Table 1 Position, electrode number and root mean square errors of the eight ERT profiles (D: discarded)

Cave	Position	N. electrodes	RMS error 2018	RMS error 2019
GH	Backwall	26 (1.5 m)	3.6%	7.3%
GH	Outer recess	20 (1.14 m)	2.0%	22.5% (D)
LH	Outer recess	35 (2.04 m)	9.9%	73.5% (D)
LH	Outside	35 (2.04 m)	8.2%	8.0%
BH	Backwall	35 (2.04 m)	88.6% (D)	168.7% (D)
BH	Outer recess	35 (2.04 m)	9.9%	97.0% (D)
TE	Backwall	35 (2.04 m)	3.6%	9.1%
TE	Outer recess	35 (2.04 m)	2.3%	1.2%

are commercially available and have been used in the context of building stone and built heritage studies e.g. by [36] and [37]. We used the MOIST 350B sensors manufactured by hf sensor (Leipzig, Germany) which generate an electromagnetic wave in a frequency range of 2–3 GHz and measure the proportion of reflected energy ("reflection coefficient"). We used two different sensor heads that penetrate to different depths (R1M: 2–3 cm; PM: 25–30 cm according to the manufacturer). The sensors measure an integrated volume from the surface down to the specified depth, so that no accurate depth for the measured signal can be given.

The MOIST 350B measures dimensionless MI (moisture index) values that are scaled from 0 (zero reflectance) to 4000 (100% reflectance). Own experience from laboratory tests show that individual calibration from MI to rock water content (RWC) is required for each type of rock; the calibration procedure is described in subsection "laboratory calibration".

At the site, grid-shaped measurement fields were recorded. Grid spacing was 20 or 40 cm wide; the number of grid points was very variable and ranged from e.g. 4×4 or 6×6 to 12×4 grid points depending on size and topography of the walls. Four measurement grids were taken in each of the four caves. All grids were measured using both sensor heads, in the following referred to as R1M(3 cm) and PM(25 cm).

Infrared thermography (IRT)

We used a VarioCAM hr (InfraTec GmbH) thermal camera with a thermal resolution better than 0.03 K (low noise detector) and a measurement accuracy of ±1.5 K. The camera works in a spectral range of 7.5–14 μm. The detector size is 640×480 infrared pixels. The camera has the option of a mechanical resolution enhancement that improves resolution to 1280×960 pixels. The emissivity value in the camera menu was set to 0.9 which is typical of natural sandstones (e.g. [38]). For a full treatment of underlying radiation physics we refer to [39] and [40].

The camera was firmly placed on a tripod in front of GH (distance of approx. 5 m to the entrance) in a way that the camera image captured the rim of the outer entrance, the inner entrance and the back wall. IRT images were automatically taken every 10 min for 24 h (=144 images). This 24-h monitoring was carried out on 27/28 March 2018 and 19/20 July 2019; we only report on the first 24-h measurement. Data was evaluated in a self-written, MATLAB-based software to extract maxima, minima, amplitudes and temperature curves over time at selectable points.

Laboratory calibration of ERT and MW

Two big stone samples were collected at the Uplistsikhe site in order to calibrate ERT and MW sensors. The stones were selected with the help of local site managers outside the excavation site (no sampling within the site allowed) and were comparable to the rock series of the investigated caves in terms of structure and texture. Based on evidence from small chipped fragments in the examined caves, it was assumed that stone 2 was more similar to the rock at the investigated caves than stone 1 according to colour and texture. This assumption proved right as calibration curves of stone 1 did not match the values measured on site, while stone 2 allowed a reasonably good calibration. Thus, only results of stone 2 are shown here.

The stones were sawn to an approximate size of $18\times18\times18$ cm^3. Four electrodes (steel screws) were installed on one side of the stone cubes in order to measure electrical resistivity in a 4-point array. The stones were oven-dried at 60 °C for a week and the dry weight was measured, then they were put in deionized water for a total of 4 days (2 days half-immersed, then 2 days immersed to the upper edge) and the wet weight was measured. For both dry and wet, five replicate readings of electrical resistivity were taken within approx. 1 min (using the same GeoTom device as in the field) and 15 measurements with both sensor heads of the MW device on three sides of the stones (5 on each side). After that, the stones were adjusted (by slow drying) to a water content of 50% saturation; stones were wrapped in plastic foil for some days to allow for even distribution of the pore water. Then resistivity and MW readings were taken at the same spots according to the same procedure.

The results of the calibration (Fig. 4) show that the conductivity-RWC relation follows a root function (cf. [29, 41]). For fitting a curve we gave more attention to the 0% and 100% values since the intermediate saturation (50%) is likely to be less reliable. This is due to uneven pore water distribution within the
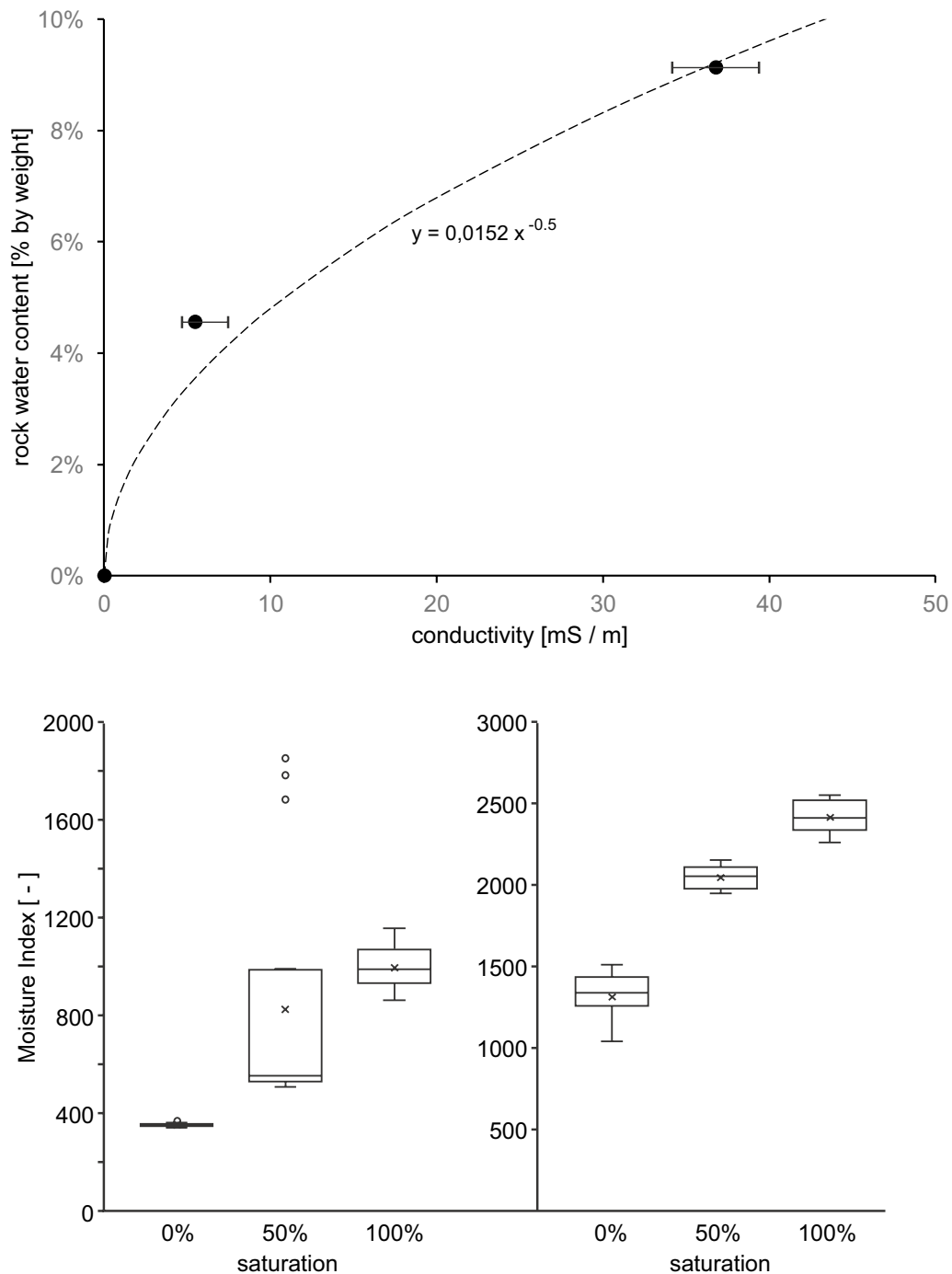
$$y = 0{,}0152\ x^{-0.5}$$

Fig. 4 Lab results for the calibration of ERT and MW measurements. Upper: conversion of electrical conductivity to rock water content (root function was chosen despite the non optimal fitting at medium saturation). Lower left: boxplots of moisture index at different saturations for MW surface sensor R1M(3 cm) (circles: outliers, see text); lower right: for MW volume sensor PM(25 cm)

sample which occurs, despite of sealing, due to gravity effects and water being retained longer in finer pores. The MW calibration show very consistent readings with the R1M(3 cm) sensor at 0%, while considerable spread occurs at 50% saturation which shows the

problem of inhomogeneous pore water distribution. Thus, we stayed with a linear calibration between 0 and 100%. If the three outliers at 50% saturation (circles in Fig. 4) are discarded, the R^2 for the linear fit is 89.5%. The inhomogeneity problem disappears for the

PM (25 cm) sensor ($R^2 = 91.5\%$); this is understandable, as the measurement averages over a larger volume. For this sensor a slightly curved calibration line would be justified. However, linear relationships between MW reflectance and RWC were recently comfirmed by [30, 36, 42, 43] and so we applied the simpler linear approach.

Both techniques have a certain temperature dependency (electrical resistivity more than microwave reflectance). For this reason, all measurements were performed in a climate cabinet at different temperatures. Since ERT profiles and MW grids were taken at specific dates and significant temperature differences between the sites are improbable, only the 20 °C calibration was used in the context of this paper. A more detailed description of the calibration process can be found in Sass et al. (in prep.).

Results

Salt distribution from paper pulp poultices, drill dust and fragments

PPP data shows that the back wall of GH is the saltiest by far (mean: 742 µS/cm) (Fig. 5). GH outer recess (88 µS/cm without outlier), LH outer recess (127 µS/cm) and TE outer recess (124 µS/cm) show significantly lower conductivity. Salt concentration at TE backwall is slightly higher compared to the aforementioned sites (275 µS/cm). Elevated conductivity at GH backwall is mainly found in the upper parts of the wall and correlate with visible zones of salt efflorescence. The only salty patch at GH outer recess is close to a joint with signs of moisture seepage. At TE backwall, the saltiest zone is near diagonal joints, also with signs of seepage. This is an indication that the salts come out of the rock with seepage water and do not derive from direct atmospheric deposition.

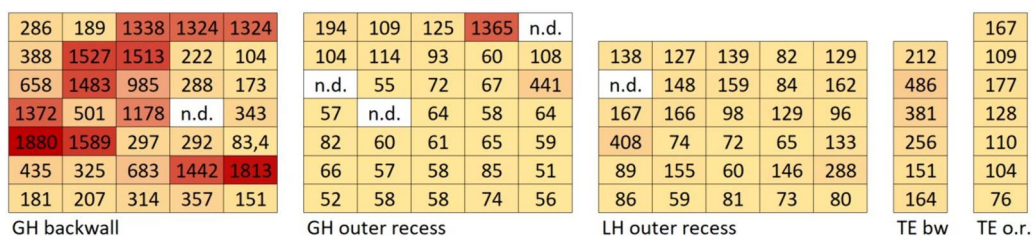Drill dust samples show that at almost all sites, significant concentrations of salt are only found at the

Fig. 5 Spatial distribution of PPP conductivity [µS/cm] as a proxy of total soluble salt concentration. n.d.: no data
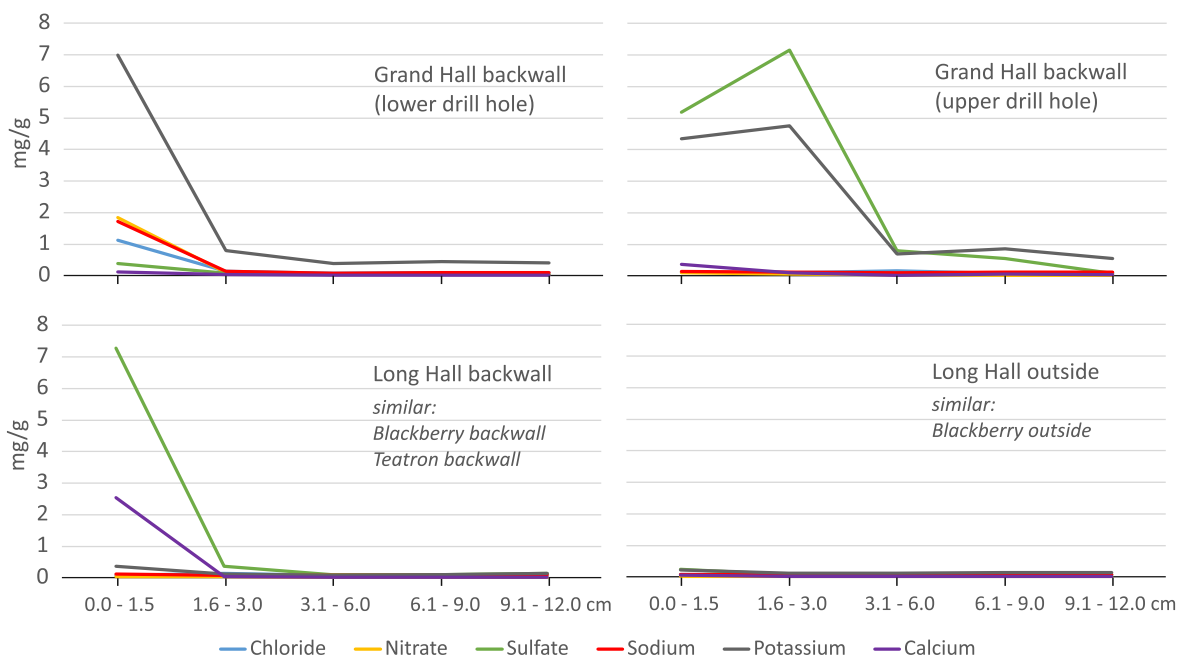

Fig. 6 Concentration of selected ions in drill dust samples

immediate surface (Fig. 6), with the exception of GH-bw-upper where high concentrations of K^+ and SO_4^{2-} reach down to 1.5–3.0 cm. All other back walls also show salts only at the surface, albeit to varying degrees (e.g. for SO_4^{2-}: LH 7.3 mg g^{-1}, BH 5.4 mg g^{-1}, TE 3.9 mg g^{-1}). At the "outside" sites of LH and BH practically no salts are detectable. LH outside is exposed to direct rainfall, so any salts that precipitate are likely to be washed off.

The most abundant anion is SO_4^{2-} with the noteable exception of GH-bw-lower where Cl^- and NO_3^{2-} are more important (Table 2). Among the cations, K^+ is the most important at GH backwall and TE backwall while Ca^{2+} dominates at BH and LH backwalls. GH lower drill hole is the only place where elevated concentrations of Na^+, Cl^- and NO_3^{2-} were found. In the collected surface fragments, K^+ and SO_4^{2-} predominate at GH backwall while Ca^{2+} and SO_4^{2+} are abundant at BH, LH and TE. At the latter sites K^+ and NO_3^{2-} also occur. The ions NH_4^+, Mg^{2+}, PO_4^{3-}, Br^- and NO_2^- are of subordinate importance in all samples and are not documented.

Main salt types given in Table 2 are derived from stoichiometric considerations and do not include double salts. In order to supplement this simplifying approach,

RUNSALT software was used to calculate the composition of different salt types that crystallize from the brine composed of the given ions. At GH-bw-lower, halite (NaCl) and niter (KNO_3) prevail. Crystallisation of NaCl occurs at < 68% RH associated with a volume increase of 0.7 to 0.9% converted to the entire sample. LH-outer-recess and BH-backwall are gypsum-dominated sites. The anhydrite-gypsum transformation takes place at 50–70% RH depending on temperature, associated with a moderate volume increase (0.2–0.25%). However, this mechanism is relevant only at geological timescales which reduces the significance of this process in the built or rock-hewn heritage context [50]. At all other sites, K_2SO_4 (arcanite) and its hydrates (e.g. $K_2SO_4 \cdot H_2O$) dominate; only minor shifts from arcanite to its hydrates occur (sometimes combined with Ca in the crystal lattice) without any volume increase or decrease.

MW-handheld results

The range of the measured MW values in the field matched the range of the laboratory calibration very well. Walls that were estimated to be very dry in the field, actually showed readings close to the "zero

Table 2 Ion concentration (mg g^{-1}) at drill hole samples (only 0–1.5 cm) and collected surface fragments

Site	Sample	Cl^-	NO_3^{2-}	SO_4^{2-}	Na^+	K^+	Ca^{2+}	Salt types[a]
a) Drill samples								
GH-bw lower	0–1.5 cm	1.12	1.85	0.39	1.72	6.99	0.12	*NaCl, KNO₃*
GH-bw upper	0–1.5 cm	0.13	0.11	5.18	0.14	4.34	0.36	*K₂SO₄*
LH-backwall	0–1.5 cm	0.08	0.03	7.29	0.12	0.37	2.55	*CaSO₄*
LH-outside	0–1.5 cm	0.07	0.02	0.24	0.09	0.22	0.05	*K₂SO₄*
BH-backwall	0–1.5 cm	0.08	0.03	5.37	0.12	0.65	1.86	*CaSO₄ (K₂SO₄)*
BH-outer-rec	0–1.5 cm	0.08	0.04	0.86	0.11	0.55	0.25	*K₂SO₄ (CaSO₄)*
T-backwall	0–1.5 cm	0.08	0.04	3.94	0.13	1.57	0.67	*K₂SO₄, CaSO₄*
T-outer-rec	0–1.5 cm	0.07	0.03	1.70	0.11	0.50	0.52	*K₂SO₄, CaSO₄*
b) Surface fragments								
GH-backwall	SF1	0.03	0.17	27.78	1.19	15.54	0.04	*K₂SO₄*
GH-bw upper	SF3a	0.03	0.39	30.99	0.63	18.75	0.03	*K₂SO₄*
GH-bw upper	SF3b	0.05	0.15	30.30	2.17	16.36	0.02	*K₂SO₄*
GH-bw lower	SF4a	0.39	0.63	29.84	0.18	18.38	0.04	*K₂SO₄*
GH-bw lower	SF4b	0.29	3.04	24.45	1.76	15.46	0.03	*K₂SO₄*
GH-bw corner	SF5	0.16	1.75	22.55	1.68	11.55	0.71	*K₂SO₄, CaSO₄*
BH-bw soot	SF6	0.02	0.11	5.56	0.10	0.90	1.70	*CaSO₄*
BH-outer-rec	SF7	0.06	10.96	10.43	0.39	13.71	0.06	*K₂SO₄, KNO₃*
TE-outer-rec	SF8	0.03	3.35	4.73	0.08	2.55	1.19	*CaSO₄, KNO₃*
TE-backwall	SF9	0.03	3.89	7.67	0.20	7.29	0.09	*K₂SO₄, KNO₃*
LH-outer-rec	SF10	0.02	0.36	5.89	0.63	1.87	0.93	*K₂SO₄, CaSO₄*
LH-outer-rec	SF11	0.34	2.64	13.60	0.66	5.26	1.72	*CaSO₄, KNO₃*
LH-outer-rec	SF12	0.16	14.57	5.56	0.17	8.66	1.10	*CaSO₄, KNO₃*

The combination of K_2SO_4 and $CaSO_4$ may also point to potassium calcium sulphate (syngenite)

[a] probable main salt types based on stoichiometric considerations

moisture" values from the laboratory. Few values were slightly negative after applying the calibration (down to -10% saturation) which shows that one rock sample cannot fully represent the natural variability in the field. Maximum values (apart from few single outliers) were at around 70–80% saturation. The mean saturation over all test fields was 15% for sensor R1M(3 cm) and 18% for sensor PM(25 cm) which appears to be realistic as the conditions in October 2022 were very dry.

Mean values for each grid are compiled in Table 3. Deep values from PM(25 cm) were more variable than surface readings from R1M(3 cm). For PM(25 cm), highest mean values were recorded for the ceiling positions (33%), followed by back walls (23%), semi-open niches (12%) and outside positions (3%). The order for R1M(3 cm) is the same with less spread (20%, 18%, 12%, 10%). There are no significant differences between the caves for R1M(3 cm), and slightly higher mean values for PM(25 cm) at LH and TE compared to BH and GH. At BH middle and BH outer recess, the upper half of the grids was slightly wetter than the lower half.

The effect of salt efflorescence on MW values was tested by comparing the readings from these areas to areas without visible salt. Areas of salt efflorescence inside the caves were found to be drier on average (e.g. GH ceiling: mean without salts: 45%, mean with salt efflorescence: 27%). There was no detectable effect of soot cover on moisture readings.

Table 3 Mean saturation values for the 16 grids measured with the two MW sensors RM1 and PM

Measurement grid	R1M (3 cm) (%)	PM (25 cm) (%)
BH backwall	17	16
BH ceiling	20	18
BH middle	12	15
BH outer recess	9	4
GH backwall	12	18
GH ceiling	20	38
GH outside middle	6	−2
GH outside left	8	−8
LH backwall	18	25
LH ceiling	18	30
LH outer recess	15	19
LH outside	19	23
TE backwall	23	32
TE ceiling	23	45
TE outer recess	10	9
TE outside left	9	−1

Moisture patterns at the back walls and ceilings of GH and TE are displayed in Fig. 7. Surficial moisture [R1M(3 cm)] is low and quite homogeneous at both sites, the ceilings are slightly wetter than the back walls. An outlier of 100% saturation at TE may be thought being a measurement error, but correlates exactly with the maximum value in the deeper layer and was therefore left in place. In the deeper layer [PM(25 cm)], well-defined areas of increased moisture can be observed. At GH, a moist zone extends diagonally across the left part of the ceiling. At TE, the moist zone is half at the ceiling and half at the back wall where it extends above a pronounced, mossy fissure that appears to dam seepage water, some of which seeps out at the surface ("outlier" close to a mossy patch). Both moist zones are not clearly recognisable at the surface which shows that the rock was dry at the surface at the time of measurement (autumn) and the seepage water had retreated 1–2 decimetres into the rock in most places. All other plots in the other caves were much more homogeneous and mostly dry.

ERT results

2D-sections of moisture content were calculated from the ERT resistivity profiles (Fig. 8) using the calibration curve of Fig. 4a. Calculated water content ranges from almost nil up to approx. 20% RWC, small areas reach up to 40% at GH backwall. Spatial distribution is very variable, particularly near the surface. Moisture distribution differs between the sites. GH backwall stands out for a thin wet layer at the surface (cf. Figure 8); the high values here exceed the estimated pore volume which suggests that the visible salt efflorescence on the surface contributes to increased conductivity. It is not possible to separate water content and salinity as reasons for increased conductivity because these two factors are closely interrelated. However, the conductive surface layer had almost disappeared in summer 2019, and thus it is highly probable that higher dampness in spring 2018 caused the conductivity peak. GH outer recess is two-part with pronounced wetness in the upper part of the profile; from field evidence it seems that precipitation water seeps down from the roof of the cave through cracks and over the surface. At TE backwall, TE outer recess and LH outside, the base of the profiles is clearly wetter which points to capillary rise of moisture. In most cases, cracks are visible as very dry zones at the surface, e.g. at TE backwall 0.6 m, while they are not discernable any more at greater depth. The moist zone of TE backwall at 0.2–0.5 m matches the moist zone above the cracks in the MW sensor data (Fig. 7).

The 1D-depth profiles of Fig. 9 were generated by calculating the mean RWC of each ERT model layer. The horizontal lines show that there is not much change of RWC deeper than approx. 10 cm. Only LH outer recess
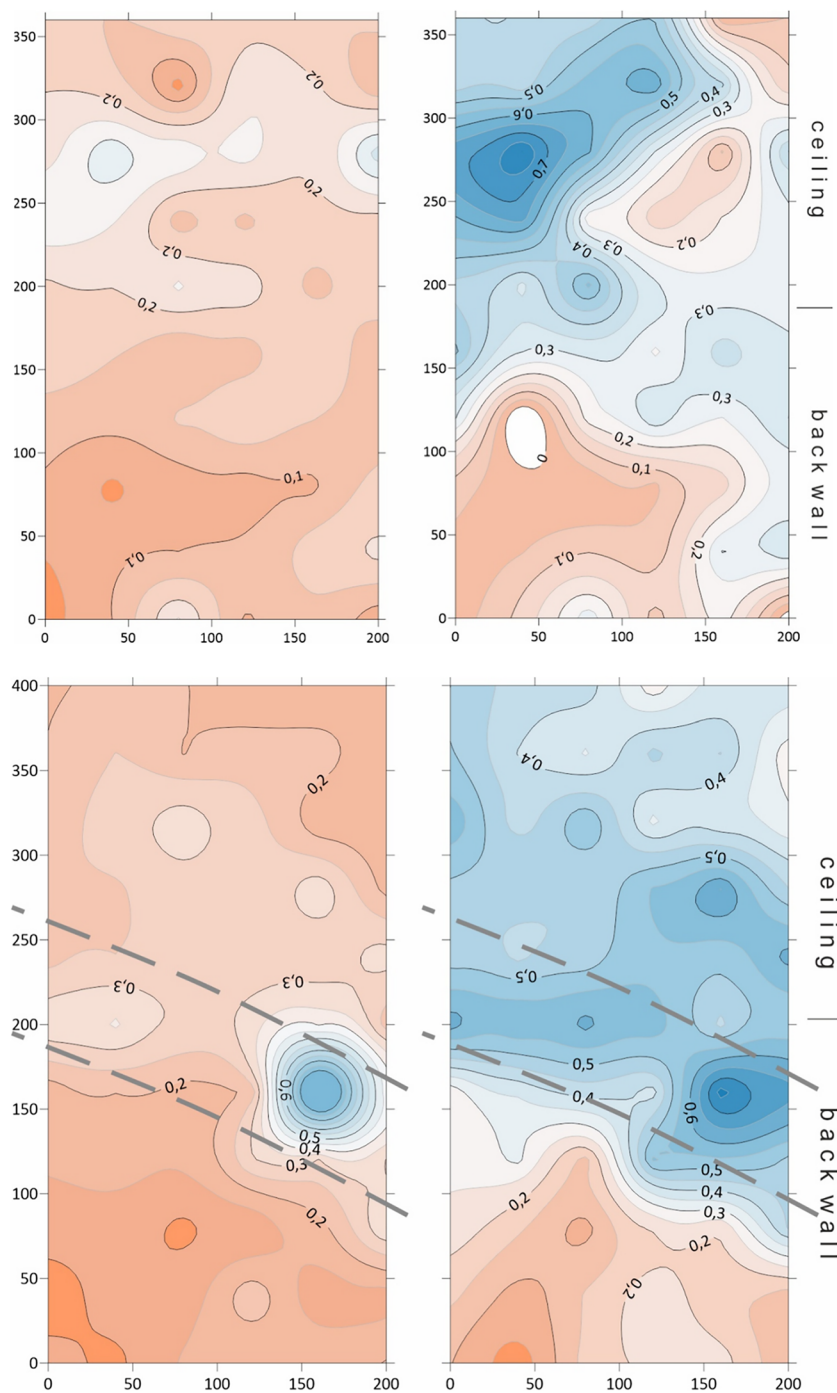
Fig. 7 Moisture distribution derived from handheld MW sensors. Left: surface sensor R1M(3 cm), right: deep sensor PM(25 cm). Upper: GH backwall and ceiling; lower: TE backwall and ceiling (dashed lines: prominent joints). Back walls and ceilings are connected without sharp angle in a quasi-continuous transition

and TE backwall are a little more moist inside which could point to water originating from the inner rockwall or the surface above. Towards the rock surface, variability is higher. The "outer recess" sites of BH, GH and LH were

slightly dried out at the surface, probably due stronger evaporation than fully inside the caves. At LH outside, a "bump" of RWC between 5 and 15 cm depth may be an indication of a rainfall event in the days preceding the
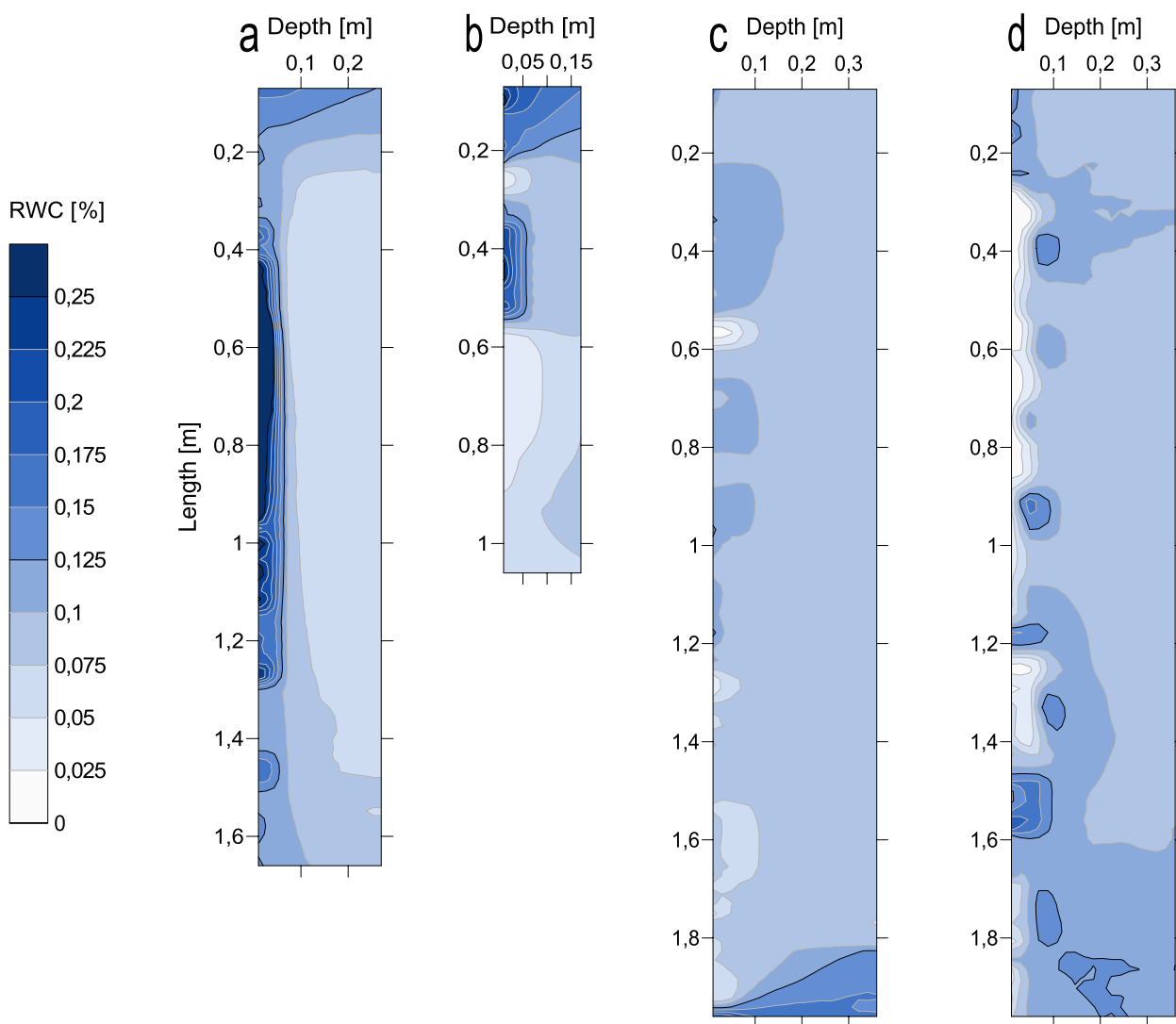
Fig. 8 RWC distribution derived from 2D-resistivity at four exemplary profiles. Respective surfaces on the left. **a** GH backwall; **b** GH outer recess; **c** TE backwall; **d** LH outside

measurement. The reason for the relatively high RWC at the surface of TE outer recess is not clear as the site appears to be shielded from most rainfalls. Increasing moisture towards the surface at LH outer recess and TE backwall might be due to surface condensation because of temperature differences or hygroscopic effect of salts. This reason is evident for GH backwall, where visible wetness was observed and salts might contribute to high conductivities.

Of the four usable profiles (in terms of data quality) from 2019, three are very similar to those from summer 2018 (LH and TE outer recess, TE backwall; these are not presented). At GH backwall, the markedly increased RWC at the surface had totally disappeared in 2019

(which matches the field impression). Apparently, the preconditions for air humidity condensation were not met anymore (see Discussion).

IR thermography

At both monitoring dates (March 2018 and July 2019), mean temperatures were lowest in the innermost chamber of GH, higher in the middle part of the cave and highest at the outer edge (Fig. 10a). Also at both dates, minimum temperatures were lowest in the inner chamber and slightly higher in the middle cave. The lowest stripe of the back wall cools down the most, which makes it the area which is probably most affected by condensation of air humidity. In July 2019 the outer rim was cooler
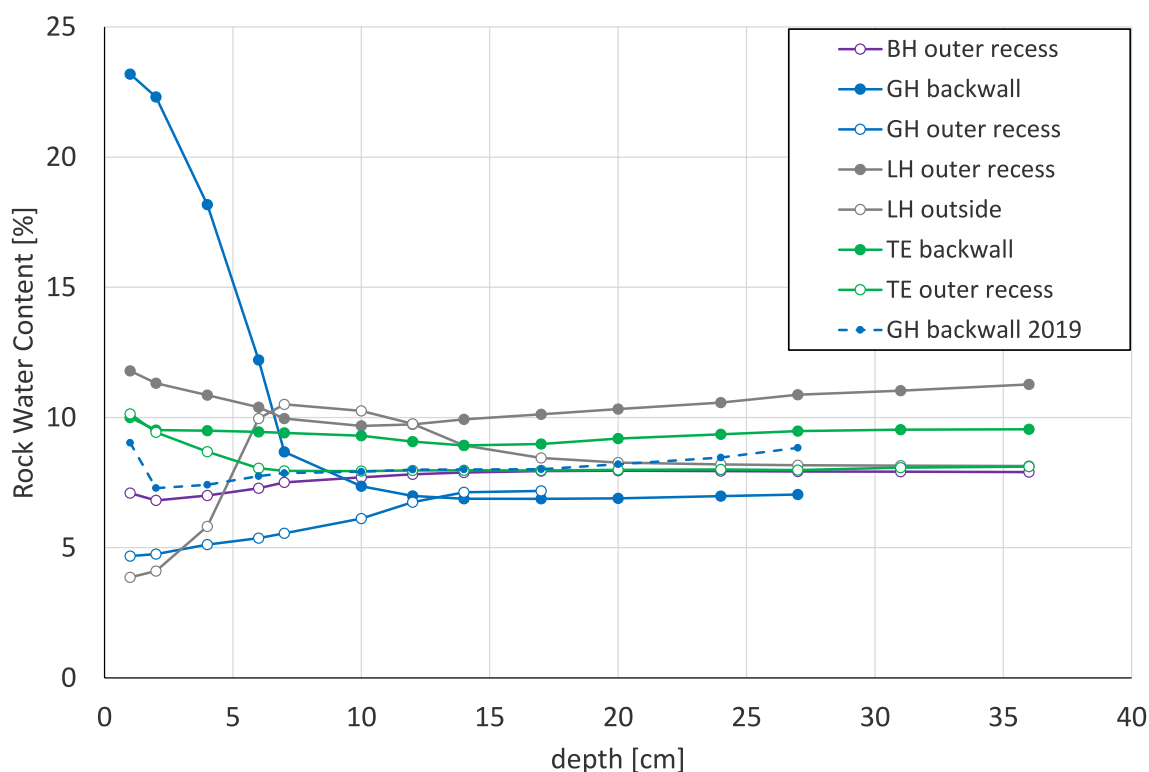
Fig. 9 1D-depth profiles of RWC derived from numerical analysis of the geoelectrical profiles

due to outgoing radiation (Fig. 10b), while in March 2018 under slightly overcast sky, contrast between inside and outside was low (not shown). Visible salty scales unter the cave ceiling have cooler minima, probably because of lacking thermal contact to the main rock body.

Figure 10c shows the cumulated temperature change ($|\Delta T|$) over the 144 images. The outer rim shows the highest fluctuation and the inner cave the lowest, but it is also evident that the mentioned salty flakes at the cave ceiling show higher fluctuation than their surrounding, which could drive their detachment. Figure 10d shows temperature curves for six selected positions marked in Fig. 10a. Point 1 (right edge of the outer rim) shows the largest amplitude due to direct sunlight in the afternoon. Amplitudes and mean temperatures decrease towards the inner chamber (points 2–5) and are lowest at its base (point 6). The difference between the salty scales (point 4) and their surrounding can be traced: In the warm hours of the day, short-term fluctuations are stronger on the scales, while in the night time they cool off more strongly (as mentioned for Fig. 10b).

Discussion
Validity of the approach
All methods applied delivered valuable and partly complementary results. ERT was at the edge of its applicability, particularly on the dry surfaces in summer 2019. Calibration is imperfect as rock samples, even of considerable size, cannot fully reproduce the conditions of an inhomogeneous rockwall. Nevertheless, relative tendencies (higher or lower) and the approximate degree of saturation can be estimated. It would have been desirable to have all methods applied at all three fieldwork dates; however, this was not possible due to technical and organisational issues. The use of MW handheld sensors in autumn 2022 appeared to be particularly promising and it would have been beneficious to have comparable measurements from spring and summer.

Sources of moisture
Regardless of the limitations mentioned above some general patterns of moisture distribution can be observed. There is evidence of more than one pathway of water infiltration. In spring 2018, the surfaces (outer 0–10 cm) of the cave walls were moister than the deeper layers (ERT, Fig. 9). This means that an external source of moisture is more probable than seepage water from the inside, pointing to condensation of air humidity on the comparatively cool cave walls. Particularly in spring, temperatures at the back walls can be several degrees cooler than the outside air temperature (IRT results, Fig. 10) so that the dew point can be undershot. Condensation may
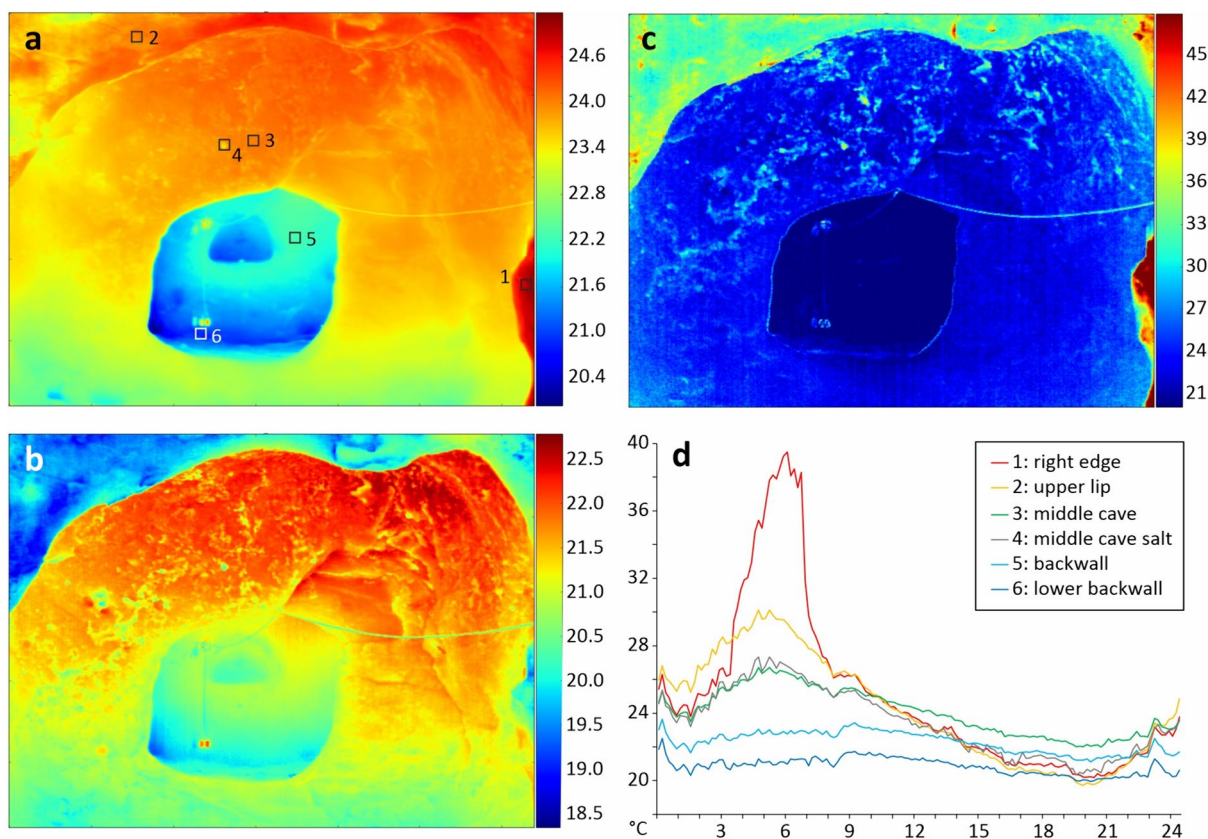
Fig. 10 Results of the IRT 24-h monitoring of July 2019. **a** mean T over 24 h; **b** minimum T over 24 h; **c** accumulated modulus of 10-min T fluctuation over 24 h; **d** T graphs at the six positions marked in (**a**). Height of the inner entrance approx. 1.7 m

be facilitated by salt efflorence of NaCl and associated hygroscopicity effects (see below) so that the immediate dew point need not be reached. Condensation as the primary source of moisture has recently been reported by Ouyang et al. (2023) for a sandstone cave in China. The temporal fluctuation of RWC at Uplistsikhe as measured with microwave monitoring also shows moisture increase in time periods of dew point undershoot (second paper in preparation).

In autumn after a long period of dry weather, rock surfaces have dried out, particularly at sun- and wind-exposed sites outside the caves but also inside the chambers as shown by MW (Table 3). Thus, the moisture gradient has reversed from moist surface – drier inside (spring) to dry surface – moister inside (autumn). This is particularly the case at the roofs of the inner chambers where seepage water percolates through the rock, and most strongly at spatially confined locations where seepage is channelled through fissures (ceilings of GH and TE) (Fig. 7). The findings from the MW measurements are supported by the confined moist zone in the ERT profile on TE backwall (Fig. 8c, 0.2–0.5 m). ERT of LH outer recess may also indicate water coming from inside

the rock along confined waterways. Thus, seepage locally is an important source of moisture that becomes more significant when the season of air humidity condensation is over. The overarching role of fissures as pathways of infiltration and percolation has been shown at various heritage sites (e.g. [44, 45]). The opposite effect can be seen at TE outer recess (Table 3): This site has no connection to the inner rock due to a cave behind it and is shielded from rain, thus it is very dry.

Near the facades of the caves, direct rainfall and channeled runoff from precipitation is another important moisture source, as ERT profile GH outer recess shows (Fig. 8b) (also [44, 45]). At this site water is coming from the top, probably facilitated by the presence of joints, and creeping down on the surface. For LH outside, spatially limited moist areas are also likely to derive from rainfall, while the surface is dried out by sun and wind (Fig. 8c).

Finally, microwave monitoring at GH backwall shows that moisture increases after long rainfalls at the base of the wall rather that at the top (second paper in preparation). The ERT profiles LH outside and also TE backwall are slightly wetter at base. This points to capillary rise from a rising slope water table (Fig. 8c, d). Figure 11
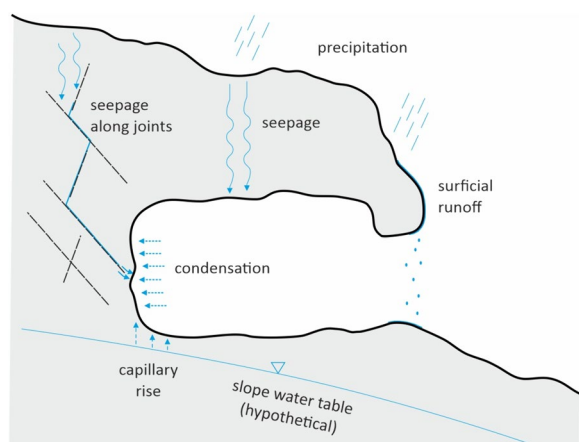
Fig. 11 Hypothetical sketch of the different pathways of water ingress at a typical cave. Not all moisture sources occur in all caves

summarises and visualises the possible sources of moisture.

Sources of salts

The spatial distribution of salts gives no direct indication of their origin. Salts either derive from the in situ rock or they are legacy from air pollution around the town of Gori. Dominating sulphates point to an influence of air pollution. It is somewhat uncommon that potassium sulphate (K_2SO_4) dominates over Na_2SO_4 which is agreed to be one of the most common and destructive salts at buildings [5, 46, 47]. Potassium sulphate is present in agricultural fertilizers [48]; however, this source seems to be unlikely here regarding the steep topography and rocky surface of the site. Thus, an in situ origin of K^+ ions (e.g. from potassium feldspar) seems to be more probable. Gypsum ($CaSO_4$) may be formed by sulphuric deposition combined with the partly calcareous matrix of the bedrock. The combination of K_2SO_4 and $CaSO_4$ at several sites (Table 2) may point to the double salt potassium calcium sulphate (syngenite). Syngenite was also found in black crusts of monuments in Serbia due to the presence of K-feldspar [48]. NaCl was found in drill samples and surface fragments of GH backwall (Fig. 6, Table 2). Its origin is unclear as no significant amounts of soluble salts in the rock were reported by geologists (e.g. [18]); however, unreported sea salt deposits as thin layers in the sandstone cannot be completely ruled out. Furthermore, in Uplistsikhe concrete was largely used to reinforce ceilings in several caves and also to seal deep cracks on near-horizontal open spaces of bedrock surface (M. Elashvili, oral comm.). Even though NaCl is not a typical component of concretes, this type of local anthropogenic source seems the most likely.

Distribution and phase changes of salts

Drill hole samples show salt crystallisation at the immediate rock surface (Fig. 6). This pattern occurs after evaporation of surface-wetted rock, provided that "the rate of evaporation is lower than the potential rate of outward salt solution migration" ([49], p. 80 f.). This is probably the case in the caves where seasonal surface-wetting occurs by condensation and the evaporation rate in the shielded caves is low. Parsons and Abrahams [50] also point out that if the drying rate is lower than moisture replenishment from within the stone, efflorescence of crystallised salts will occur at the surface. At sites outside and above the caves (e.g. Figure 1b), faster evaporation occurs and the salt crystallization horizon is accordingly deeper, leading to blistering of cm-thickness. Generally, caves are preferred places for salt crystallisation due to slow drying and lateral salt migration as shown by [51] for tafoni.

The finding from MW measurements that some areas of salt efflorescence in the caves are drier than their surrounding might be due to gypsum precipitation that can reduce the drying rate of porous stone due to accumulation at the evaporation front and associated pore clogging [52]. However, the reasoning may be vice versa: At places that remain moist also in the dry season due to seepage, salts cannot crystallise while in the surrounding, the rock slowly dries out and salts can precipitate at the surface. Direct thermal signals of salt crystallisation were not detected in the IR thermal data; however, the thermal signature e.g. of KNO_3 crystallization proved to be too week to be registered by IR even under controlled laboratory conditions [53].

While sodium sulphate is generally agreed to be one of the most damaging salts at porous rocks [5, 47], not much is published on the damaging potential of potassium sulphate. Its deliquescence point is at 97–99% RH [54] in the temperature range encountered at the site so that not many deliquescence-crystallisation cycles are to be expected. This is supported by the RUNSALT model indicating that the K_2SO_4-dominated sites are rather inactive in terms of salt weathering. Inconsistencies of RUNSALT regarding the exact crystallisation points of the hydrates of potassium sulphate [27] do not affect this assessment. Efflorences of syngenite and gypsum were also found by [55] at a cave site in calcarenite bedrock, with some effect on rock microporosity.

The critical deliquescence point of NaCl is at around 75% RH depending on temperature [56]. Mean relative humidity at the meteorological station of Uplistsikhe was 68% from Aug 2019 to Jul 2021 and ca. 75% in the winter months. In the mentioned 2 years, diurnal crossing of the 75% threshold occurred on 548 days (= three of four days). Thus, diurnal crystallisation cycles may occur over

long periods of the year. According to the literature, NaCl does not produce important damage to the stone apart from efflorescences at the surface [46]. However, slightly erosive effects of NaCl were stated by [47], and sodium chloride was found to disintegrate sandstone samples by crystallisation pressures (Levin, 1982, cited from [6]). Cardell et al. [12] pointed out that condensation is conducive to crystallisation weathering as it can form a brine solution that migrates towards the inside of the stone [57]. We assume that in the annual cycle, enrichment of NaCl at the surface occurs during long periods of summer drying, while condensation and frequent crystallisation cycles occur in winter. NaCl crystallisation near the surface can explain the widespread flaking at the GH site (Fig. 1a) [12, 58]. We further assume that GH backwall is wetter than all other sites because of hygroscopic NaCl and KNO_3 (drawing water at > 75% RH) while the other sites are drier because the prevailing K_2SO_4 and $CaSO_4$ have their deliquescence points at 99% or higher [52, 54].

Gypsum is one of the most common salts found at rock-hewn heritage sites but is considered less aggressive than other salts [5, 52]. The only places were gypsum seems to be the only significant salt are the black-crusted backwalls of BH and LH (Table 2) which appear to be relatively stable indeed. However, in mixed solutions with halite, the deliquescence humidity of gypsum is lowered to approx. 85% [47]. Gypsum-anhydrite transition is at around 42 °C [52] which is a possible temperature on sun-exposed rock at the site, but not within the caves. However, gypsum-anhydrite transition can occur at lower temperatures due to RH fluctuations between approx. 60 and 100% RH ([52], Fig. 3) but is rather slow. In mixed salt solutions, nitrates as well as halite tend to keep moisture in the material because of their deliquescent nature. This allows for an increased migration of less soluble gypsum; the damage from these combinations have been found in practice (e.g. [59]). Thus, we assume that gypsum in combination with available halite and niter contributes to increased weathering at GH.

Conclusions

The combination of rock/salt sampling and moisture measurement by ERT and MW sensors revealed a complex pattern of salt and moisture distribution at the Uplistsikhe cave town site. Summing up, four possible sources of moisture can be evidenced depending on season and spatial situation: condensation, seepage, precipitation and capillary rise. Of these, condensation (in spring) at some of the cave backwalls and seepage (directed by the fissure network and assumedly mostly during long rainfalls in winter) are the most important. For site conservation this means that water ingress above

caves at risk should be prevented, rather than applying surface treatments in the caves themselves.

In the caves, salts concentrate at the surfaces due to slow evaporation. K_2SO_4 and $CaSO_4$ are the most important salts over most of the site. GH stands out for NaCl efflorescence which facilitates condensation and increases the weathering effectivity of gypsum. This combined effect is probably responsible for widespread, but shallow flaking at this site. Flaking is favored by increased temperature fluctuations on detached scales. Blistering of thicker layers rather occurs outside of the caves due to stronger evaporation.

Combined results of moisture and salt distribution can potentially explain most of the weathering patterns found at rock-hewn heritage sites. At Uplistsikhe, further investigations are necessary, in particular on the origin of the salts encountered and on seepage intensity at different locations and in different seasons.

Author contributions
SH carried out approx. 80% of the field work, including salt sampling and analysis. ERT and IRT were jointly performed by SH and OS. Microwave measurements including lab calibration were carried out by OS. The paper was entirely written and revised by OS because SH left the university.

Availability of data and materials
Data will be made available upon reasonable request.

Declarations

Ethics approval and consent to participate
Not applicable.

Competing interests
The authors declare no competing interests.

References
1. Sass O, Viles H. Heritage hydrology: a conceptual framework for understanding water fluxes and storage in built and rock-hewn heritage. Herit Sci. 2022. https://doi.org/10.1186/s40494-022-00693-7.
2. Heinrichs K. Diagnosis of weathering damage on rock-cut monuments in Petra. Jordan Env Geol. 2008;56:643–75. https://doi.org/10.1007/s00254-008-1358-1.
3. Saleh M. Honeycomb weathering of sandstone outcrops at Al-Hijr (Mada'in Salih), Saudi Arabia. Egypt J Archaeol Restor Stud. 2013;3:85–93.

4. Zhang Z, Yang Z, Wang S, Zhang L. Weathering rates of a sandstone structure in a semi arid environment: a case study of the ancient city of Pingyao (world cultural heritage), China. Bull Eng Geol Environ. 2011;70:231–7. https://doi.org/10.1007/s10064-010-0316-9.

5. Goudie A, Viles H. Salt weathering hazards. Chichester: Wiley; 1997.

6. Oguchi CT, Yu S. A review of theoretical salt weathering studies for stone heritage. Prog Earth Planet Sci. 2021;8:1–23. https://doi.org/10.1186/s40645-021-00414-x.

7. Franzoni E. Rising damp removal from historical masonries: a still open challenge. Constr Build Mater. 2014;54:123–36. https://doi.org/10.1016/j.conbuildmat.2013.12.054.

8. Franzen C, Mirwald PW. Moisture content of natural stone: static and dynamic equilibrium with atmospheric humidity. Env Geol. 2004;46:391–401. https://doi.org/10.1007/s00254-004-1040-1.

9. Ouyang K-G, Jiang X-W, Mei G, Yan H-B, Niu R, Wan L, Zeng Y. Physics-informed machine learning for understanding rock moisture dynamics in a sandstone cave. Hydrol Earth Syst Sci. 2023;27:2579–90. https://doi.org/10.5194/hess-27-2579-2023.

10. Blocken B, Derome D, Carmeliet J. Rainwater runoff from building facades: a review. Build Environ. 2013;60:339–61. https://doi.org/10.1016/j.buildenv.2012.10.008.

11. Benavente D, Pla C, Gil-Oncina S, Ruiz MC, Blanco-Quintero IF, Huesca-Tortosa JA, et al. Air quality monitoring for preventive conservation of the built heritage deteriorated by salt crystallization. Geosciences. 2022;12:325. https://doi.org/10.3390/geosciences12090325.

12. Cardell C, Delalieux F, Roumpopoulos K, Moropoulou A, Auger F, van Grieken R. Salt-induced decay in calcareous stone monuments and buildings in a marine environment in SW France. Constr Build Mater. 2003;17:165–79. https://doi.org/10.1016/s0950-0618(02)00104-6.

13. Marszałek M, Alexandrowicz Z, Rzepa G. Composition of weathering crusts on sandstones from natural outcrops and architectonic elements in an urban environment. Environ Sci Pollut Res Int. 2014;21:14023–36. https://doi.org/10.1007/s11356-014-3312-y.

14. Grøntoft T, Cassar J. An assessment of the contribution of air pollution to the weathering of limestone heritage in Malta. Environ Earth Sci. 2020;79:1–16. https://doi.org/10.1007/s12665-020-09027-x.

15. Egartner I, Sass O, Viles H, Dietzel M. A multi proxy investigation of moisture, salt, and weathering dynamics on a historic urban boundary wall in Oxford, UK. Stud Conserv. 2020;65:172–88. https://doi.org/10.1080/00393630.2019.1628480.

16. Orlowsky J, Groh M, Braun F. About the effectiveness of a hydrophobic surface treatment of Baumberger Sandstones. Environ Earth Sci. 2022;81:1–11. https://doi.org/10.1007/s12665-022-10186-2.

17. UNESCO World Heritage Convention. Uplistsikhe cave town. 2007. https://whc.unesco.org/en/tentativelists/5234/.

18. Popov SV, Aleksandrova GN, Voronina AA, Zaporozhets NI, Golovina LA, Koiava KP. Paleontological and lithological characteristics of the lower miocene stratotype sections of the Eastern Paratethys (Kartli Depression, Georgia). Stratig Geol Correl. 2022;30:408–30. https://doi.org/10.1134/S0869593822050057.

19. meteoblue.com. Simulated historical climate & weather data for Gori. 2023. https://www.meteoblue.com/de/weather/historyclimate/climatemodelled/gori_georgia_614455. Accessed 28 Dec 2023.

20. ICOMOS. Illustrated glossary on stone deterioration patterns: English-french version = Glossaire illustré sur les formes d'altération de la pierre : version anglais-français. Paris: ICOMOS; 2008.

21. Vergès-Belmin V, Siedel H. Desalination of Masonries and monumental sculptures by poulticing: a review. Restor Build Monum. 2005;11:391–408.

22. Egartner I, Sass O. Using paper pulp poultices in the field and laboratory to analyse salt distribution in building limestones. Herit Sci. 2016. https://doi.org/10.1186/s40494-016-0110-5.

23. Lubelli B, van Hees RP. Desalination of masonry structures: fine tuning of pore size distribution of poultices to substrate properties. J Cult Herit. 2010;11:10–8. https://doi.org/10.1016/j.culher.2009.03.005.

24. Martinho E, Alegria F, Dionisio A, Grangeia C, Almeida F. 3D-resistivity imaging and distribution of water soluble salts in Portuguese Renaissance stone bas-reliefs. Eng Geol. 2012;141–142:33–44. https://doi.org/10.1016/j.enggeo.2012.04.010.

25. Price CA. An expert chemical model for determining the environmental conditions needed to prevent salt damage in porous materials: protection and conservation of the European cultural heritage: European

Commission Research Report No 11, (Protection and Conservation of European Cultural Heritage). London; 2000.

26. Bionda D. RUNSALT-A graphical user interface to the ECOS thermodynamic model for the prediction of the behaviour of salt mixtures under changing climate. 2005. http://science.sdf-eu.org/runsalt/.

27. Godts S, Steiger M, Orr SA, Stahlbuhk A, Desarnaud J, de Clercq H, et al. Modeling salt behavior with ECOS/RUNSALT: terminology, methodology, limitations, and solutions. Heritage. 2022;5:3648–63. https://doi.org/10.3390/heritage5040190.

28. Schrott L, Sass O. Application of field geophysics in geomorphology: advances and limitations exemplified by case studies. Geomorphology. 2008;93:55–73. https://doi.org/10.1016/j.geomorph.2006.12.024.

29. Archie GE. The electrical resistivity log as an aid in determining some reservoir characteristics. Trans Am Inst Min Metall Eng Petroleum Div. 1942;146:54–62.

30. Sass O. Investigating rock moisture at a sandstone massif in the Saxonian Switzerland climbing area. jgeomorphology. 2022. https://doi.org/10.1127/jgeomorphology/2022/0711.

31. Telford WM, Geldart LP, Sheriff RE. Applied geophysics. 2nd ed. Cambridge: Cambridge Univ. Pr; 2004.

32. Loke MH. Electrical imaging surveys for environmental and engineering studies, a practical guide to 2-D and 3-D surveys. Copyright by M.H. Loke. Penang (Malaysia); 1999.

33. Loke MH, Barker RD. Least-squares deconvolution of apparent resistivity pseudosections. Geophysics. 1995;60:1682–90. https://doi.org/10.1190/1.1443900.

34. Vermeulen C, Hancke GP. Continuous measurement of moisture in nonconducting materials. IEEE Trans Instrumen Meas. 1992. https://doi.org/10.1109/imtc.1992.245105.

35. Kruschwitz S, Niederleithinger E, Trela C, Wöstmann J. Use of complex resistivity tomography for moisture monitoring in a flooded masonry specimen. J Infrastruct Syst. 2012;18:2–11. https://doi.org/10.1061/(ASCE)IS.1943-555X.0000053.

36. Orr SA, Fusade L, Young M, Stelfox D, Leslie A, Curran J, Viles H. Moisture monitoring of stone masonry: a comparison of microwave and radar on a granite wall and a sandstone tower. J Cult Herit. 2020;41:61–73. https://doi.org/10.1016/j.culher.2019.07.011.

37. Weiss T, Sass O. The challenge of measuring rock moisture: a laboratory experiment using eight types of sensors: Copernicus GmbH. Geomorphology. 2022;416. https://doi.org/10.1016/j.geomorph.2022.108430.

38. Mineo S, Pappalardo G. Rock emissivity measurement for infrared thermography engineering geological applications. Appl Sci. 2021;11:3773. https://doi.org/10.3390/app11093773.

39. Usamentiaga R, Venegas P, Guerediaga J, Vega L, Molleda J, Bulnes F. Infrared thermography for temperature measurement and non-destructive testing. Sensors. 2014;14:12305–48. https://doi.org/10.3390/s140712305.

40. Vollmer M, Möllmann K-P. Infrared thermal imaging: fundamentals, research and applications. 2nd ed. Weinheim: Wiley-VCH Verlag GmbH & Co. KGaA; 2017.

41. Sass O, Viles HA. Wetting and drying of masonry walls: 2D-resistivity monitoring of driving rain experiments on historic stonework in Oxford, UK. J Appl Geophys. 2010;70:72–83. https://doi.org/10.1016/j.jappgeo.2009.11.006.

42. Piuzzi E, Pittella E, Pisa S, Cataldo A, de Benedetto E, Cannazza G. Microwave reflectometric methodologies for water content estimation in stone-made Cultural Heritage materials. Measurement. 2018;118:275–81. https://doi.org/10.1016/j.measurement.2017.05.069.

43. D'Alvia L, Pittella E, Rizzuto E, Piuzzi E, Del Prete Z. A portable low-cost reflectometric setup for moisture measurement in cultural heritage masonry unit. Measurement. 2022;189:110438. https://doi.org/10.1016/j.measurement.2021.110438.

44. Frodella W, Elashvili M, Spizzichino D, Gigli G, Adikashvili L, Vacheishvili N, et al. Combining InfraRed thermography and UAV digital photogrammetry for the protection and conservation of rupestrian cultural heritage sites in georgia: a methodological application. Remote Sens. 2020;12:892. https://doi.org/10.3390/rs12050892.

45. Barbosa MTG, Rosse VJ, Laurindo NG. Thermography evaluation strategy proposal due moisture damage on building facades. J Build Eng. 2021;43:102555. https://doi.org/10.1016/j.jobe.2021.102555.

46. Menéndez B. Estimators of the impact of climate change in salt weathering of cultural heritage. Geosciences. 2018;8:401. https://doi.org/10.3390/geosciences8110401.
47. Alves C, Figueiredo CAM, Sanjurjo-Sánchez J, Hernández AC. Salt weathering of natural stone: a review of comparative laboratory studies. Heritage. 2021;4:1554–65. https://doi.org/10.3390/heritage4030086.
48. Matović V, Erić S, Kremenović A, Colomban P, Srećković-Batoćanin D, Matović N. The origin of syngenite in black crusts on the limestone monument King's Gate (Belgrade Fortress, Serbia) – the role of agriculture fertiliser. J Cult Herit. 2012;13:175–86. https://doi.org/10.1016/j.culher.2011.09.003.
49. Smith BJ. Weathering processes and forms. In: Parsons AJ, Abrahams AD, editors. Geomorphology of desert environments. 2nd ed. Dordrecht: Springer; 2009. p. 69–100.
50. Parsons AJ, Abrahams AD, editors. Geomorphology of desert environments. 2nd ed. Dordrecht: Springer; 2009.
51. Huinink HP, Pel L, Kopinga K. Simulating the growth of tafoni. Earth Surf Processes Landf. 2004;29:1225–33. https://doi.org/10.1002/esp.1087.
52. Charola AE, Pühringer J, Steiger M. Gypsum: a review of its role in the deterioration of building materials. Environ Geol. 2007;52:339–52. https://doi.org/10.1007/s00254-006-0566-9.
53. Vazquez P, Sartor L, Thomachot-Schneider C. Influence of substrate and temperature on the crystallization of KNO3 droplets studied by infrared thermography. Prog Earth Planet Sci. 2018. https://doi.org/10.1186/s40645-018-0229-y.
54. Greenspan L. Humidity fixed points of binary saturated aqueous solutions. J Res Natl Bureau Stand Arch Phys Chem. 1977;81A:89–96.
55. D'Angeli IM, Lacalamita M, Sasso C, Schingaro E, Parise M. Morphological and mineralogical characterization of surficial weathering on calcarenite rocks in the rupestrian system of "San Michele delle Grotte" at Gravina in Puglia (Bari, Apulia). CATENA. 2022;216:106382. https://doi.org/10.1016/j.catena.2022.106382.
56. Grossi CM, Brimblecombe P, Menéndez B, Benavente D, Harris I, Déqué M. Climatology of salt transitions and implications for stone weathering. Sci Total Environ. 2011;409:2577–85. https://doi.org/10.1016/j.scitotenv.2011.03.029.
57. de Freitas VP, Abrantes V, Crausse P. Moisture migration in building walls—analysis of the interface phenomena. Build Environ. 1996;31:99–108. https://doi.org/10.1016/0360-1323(95)00027-5.
58. Smith BJ, McGreevy JP. Contour scaling of a sandstone by salt weathering under simulated hot desert conditions. Earth Surf Proc Land. 1988;13:697–705. https://doi.org/10.1002/esp.3290130804.
59. Weber J. Salt-induced deterioration of Romanesque wall paintings in the church of St. Georgen, Styria, Austria. In: Biscontin G, Graziano L (eds). Conservation of architectural surfaces: stones and wall coverings. p. 97–103.

Publisher's Note